





Room-temperature magnetic thermal switching by suppressing phonon-magnon scatteringFanhao Zhang ¹, Lokanath Patra,¹ Yubi Chen ^{2,1}, Wenkai Ouyang,¹ Paul M. Sarte,³ Shantal Adajian ¹, Xiangying Zuo,¹ Runqing Yang,¹ Tengfei Luo,⁴ and Bolin Liao ^{1,*}¹*Department of Mechanical Engineering, University of California, Santa Barbara, California 93106-5070, USA*²*Department of Physics, University of California, Santa Barbara, California 93106-9530, USA*³*Material Research Laboratory, University of California, Santa Barbara, California 93106, USA*⁴*Department of Aerospace and Mechanical Engineering, University of Notre Dame, Notre Dame, Indiana 46556, USA*

(Received 10 January 2024; revised 4 April 2024; accepted 22 April 2024; published 6 May 2024)

Thermal switching materials, whose thermal conductivity can be controlled externally, show great potential in contemporary thermal management. The manipulation of thermal transport properties through magnetic fields has been accomplished in materials that exhibit a high magnetoresistance. However, it is generally understood that the lattice thermal conductivity attributed to phonons is not significantly impacted by the magnetic fields. In this study, we experimentally demonstrate the significant impact of phonon-magnon scattering on the thermal conductivity of the rare-earth metal gadolinium near room temperature, which can be controlled by a magnetic field to realize thermal switching. Using first-principles lattice dynamics and spin-lattice dynamics simulations, we attribute the observed change in phononic thermal conductivity to field-suppressed phonon-magnon scattering. This research suggests that phonon-magnon scattering in ferromagnetic materials is crucial to determine their thermal conductivity, opening the door to innovative magnetic-field-controlled thermal switching materials.

DOI: [10.1103/PhysRevB.109.184411](https://doi.org/10.1103/PhysRevB.109.184411)**I. INTRODUCTION**

Solid-state thermal switches with a tunable thermal conductivity have gained substantial attention in recent years due to their potential for addressing pressing challenges of thermal management in modern technologies [1]. Differing from traditional static thermal components, which typically are either thermally conductive or insulating, thermal switches offer a dynamic response to external stimuli, enabling transitions between thermally conductive and insulating states. Realizing this inherent capacity of thermal switching not only contributes to our fundamental understanding of heat carrier interactions in condensed matter systems, but also opens up technological avenues towards externally controllable heat flow. Such control is invaluable in a range of applications, from adiabatic demagnetization refrigeration (ADR) [2,3] to thermal management of electronic and energy systems [4] and thermoelectric power generation [5]. Several approaches have been explored to achieve solid-state thermal switching with various mechanisms, leveraging different types of external stimuli, including manipulating phonon transport properties [6–9] or interfacial chemical bonding and charge distribution [10] using an external electric field, utilizing large magnetoresistance of electrons under a magnetic field [11], phase transitions induced electrochemically [12], thermally [13,14] or by light [15], electrochemical intercalation [16,17], and manipulation of the displacement amplitude of atomic vibrations via hydration [18]. The underlying physics of these switching mechanisms can vary significantly, and the discovery of new

switching mechanisms can both inspire novel forms of stimuli and guide the search for new thermal switching materials.

While previous thermal switch designs have relied mainly on electric fields and electrochemical processes, magnetic-field-driven thermal switching mechanisms remain less explored. The noncontact nature of magnetic fields can be advantageous for certain applications. Moreover, magnetic thermal switches can be particularly desirable in applications where large magnetic fields are already present, such as in ADR devices. In magnetic materials, heat conduction is determined by the transport and interaction processes of electrons, phonons, and magnons. Existing thermal switching studies have focused on the impact of a magnetic field on electron transport, namely, magnetoresistance, essentially arising from the alteration of electron trajectories in the presence of the external magnetic field. Since electrons also carry heat, materials exhibiting high magnetoresistance can achieve a substantial thermal switching ratio when an external magnetic field is applied [19]. In comparison, the impact of an external magnetic field on the phononic transport properties is not as direct. Jin *et al.* showed that a diamagnetic force induced by lattice vibrations can lead to small magnetic-field-dependent changes in the phononic thermal conductivity of nonmagnetic materials at cryogenic temperatures [20]. Recent computational studies have suggested that an external field can exert an indirect influence on phonons through phonon-magnon coupling [21]. In magnetic materials, a collective excitation in the spin structure, known as a magnon, can contribute to heat conduction at cryogenic temperatures in magnetic materials [20,22–24]. Although, at room temperature, magnons contribute minimally to the overall thermal conductivity due to their short mean free path and small heat capacity [25], they can effectively

*bliao@ucsb.edu

scatter electrons and phonons and thereby indirectly modulate thermal conductivity. Previous research has investigated the phonon-magnon interaction at cryogenic temperatures, where its impact on thermal conductivity is appreciable [26,27]. In particular, previous measurements in magnetic insulators have demonstrated that suppressing the critical magnetic fluctuations with an external magnetic field near the magnetic phase transition temperature can lead to significant changes in the thermal conductivity [28–32]. The physical origin of this phenomena has been attributed to reduced phonon-magnon scattering. However, these explorations have been limited to cryogenic temperatures below 20 K and the possibility of realizing solid-state thermal switching via controlling phonon-magnon interaction has not been examined near room temperature. In addition, the existing classic theory describing the impact of phonon-magnon interaction on thermal conductivity near magnetic phase transitions by Kawasaki [33] is phenomenological, lacking the precision to unveil microscopic details of this effect. In this work, we aim to study magnetic-field-dependent thermal transport in materials with strong spin-lattice interactions, which could result in sufficiently strong phonon-magnon scatterings to realize a thermal switching effect near room temperature. In the meantime, we hope to target materials with simple chemical compositions and structures such that we could apply state-of-the-art simulation techniques to understand their phonon-magnon interactions in detail [34].

For these purposes, a suitable candidate material is elemental gadolinium (Gd), a rare-earth metal known to possess strong spin-lattice coupling [34]. The thermal conductivity of Gd has been a subject of investigation since 1964, when Araj *et al.* measured the thermal and electric conductivity of Gd without an external magnetic field. Their study highlighted the pivotal role of the magnetic transition in Gd's thermal transport [35]. Further work by Jacobsson *et al.* concluded that magnons contribute to heat conduction in Gd below its Curie temperature ($T_c = 293$ K) and that the lattice thermal conductivity strongly depends on pressure [25]. In a study conducted by Glorieux *et al.*, the thermal conductivity of Gd was measured under a modest external magnetic field (60 mT) using a photoacoustic method and was shown to change with the field strength, especially near T_c . The authors suggested that the observed changes in thermal conductivity with the applied field could be attributed to two main factors: an increase in the effective mass of conduction electrons caused by localized spins, and alterations in the density of states at the Fermi surface due to the indirect Ruderman-Kittel-Kasuya-Yosida (RKKY) exchange interaction, which is particularly significant in rare-earth materials [36,37]. However, an important aspect that was overlooked in their study was the influence of the magnetic field on phononic thermal conductivity by modifying spin-lattice coupling.

Here, we employed a customized steady-state measurement system to measure thermal and electrical conductivity of a single-crystal Gd sample at varying temperatures under an external magnetic field up to 9 T, in order to clarify the true origin of its magnetic-field-dependent thermal conductivity. We found that the thermal conductivity of Gd increases with the magnetic field strength, specifically in the vicinity of T_c , while the change decreases at temperatures away from T_c .

By isolating the electronic and phononic contributions to the thermal conductivity, we found that the phononic contribution plays a crucial role in the observed increase in the total thermal conductivity. This conclusion was further corroborated by first-principles spin-lattice dynamics (SLD) simulation, which showed that phonon-magnon scatterings play an important role in thermal transport in Gd even at room temperature. The external magnetic field reduces the magnon population and suppresses phonon-magnon scattering, leading to the increase in the thermal conductivity. Our findings provide important fundamental insights into magnetic-field-dependent thermal transport in magnetic materials and suggest that controlling phonon-magnon scattering through an external magnetic field in materials with a strong spin-lattice coupling can be a promising mechanism for solid-state thermal switching. Because materials with strong spin-lattice coupling often show a prominent magnetocaloric effect [34], our study suggests that further exploration of known magnetocaloric materials may lead to promising candidates for thermal switching applications.

II. EXPERIMENTAL METHODS

Single-crystal gadolinium (Gd) samples with 99.99% purity were obtained from Princeton Scientific. These samples were shaped into bars of dimensions $5 \times 1 \times 1$ mm³. Thermal conductivity measurements were carried out using a steady-state method in a high-vacuum (10^{-6} Torr) environment within the Quantum Design Physical Property Measurement System (PPMS) sample chamber. A resistive heater (Omega Engineering, 120 Ω strain gauge) attached to a copper plate functioned as the heat source. A copper plate positioned on an Al₂O₃ plate was affixed to a PPMS puck, acting as both a heat sink and the sample stage. Type T thermocouples, composed of 25- μ m-diameter copper-constantan wires, were custom made and used as thermometers. Silver epoxy was employed to establish all contacts. Measurements were performed at distinct temperatures ranging from 150 to 340 K and discrete magnetic fields between -9 and 9 T. A waiting period of at least 30 minutes was allowed for each temperature and 10 minutes for each magnetic field to achieve thermal equilibrium before conducting the measurements. Electrical measurements were conducted on the same sample using the same setup, with the copper plates in the heat source and the heat sink functioning as current spreaders.

III. COMPUTATIONAL METHODS

A. Spin-lattice dynamics simulations

The spin-lattice dynamics (SLD) were executed utilizing the recently integrated SPIN package within the LAMMPS software framework [38]. Exchange coupling parameters were derived utilizing the SPR-KKR package [39,40], establishing a cluster of hcp Gd crystals with a radius of 3.5 Å. These parameters were subsequently incorporated into our SLD simulations. Detailed computational parameters are outlined in our prior publication [34].

The thermal conductivity was computed utilizing a $10 \times 10 \times 10$ supercell employing the Green-Kubo formula,

$$\kappa_{\alpha\beta} = \frac{1}{k_B T^2 V} \int_0^\infty \langle J_\alpha(t) J_\beta(0) \rangle dt, \quad (1)$$

where $\kappa_{\alpha\beta}$ denotes a specific component of the thermal conductivity tensor. Here, k_B represents the Boltzmann constant, and T and V correspond to the temperature and volume of the system, respectively. Furthermore, J_α signifies the heat current component along the α Cartesian direction (x , y , or z). The angle brackets denote an ensemble average, equivalent to the time average in molecular dynamics (MD) simulations. The heat current $J(t)$ is defined as

$$\mathbf{J}(t) = \frac{d}{dt} \sum_{i=1}^N \varepsilon_i(t) \mathbf{r}_i(t), \quad (2)$$

where $r_i(t)$ represents the time-dependent coordinate of atom i , and $\varepsilon_i(t)$ signifies the site energy.

Phonon lifetimes can be quantified through the analysis of the phonon spectral energy density (SED) using the atomic trajectory data in the SLD simulation [41]. The calculation of the phonon SED involves a Fourier transformation in spatial dimensions applied to the power spectral density of atoms [41,42], as expressed by the equation

$$\psi(\mathbf{q}, \omega) \propto \frac{1}{2} \sum_{\alpha \in \{x,y,z\}} m \left| \int_0^{\tau_0} \sum_{n_{x,y,z}} \dot{\mathbf{u}}_\alpha(n_{x,y,z}, b; t) \times \exp[i\mathbf{q} \cdot \mathbf{R}(n_{x,y,z}) - i\omega t] dt \right|^2. \quad (3)$$

Here, $n_{x,y,z}$ denotes distinct unit cells within the material, and $\mathbf{R}(n_{x,y,z})$ represents the displacement vector from the referenced basis unit cell to unit cell $n_{x,y,z}$. The function $\psi(\mathbf{q}, \omega)$ can be analyzed by fitting it using a linear combination of Lorentzian functions. The peaks within this fitted function correspond to the frequencies associated with phonons. This formulation provides a detailed representation of how the energy of phonons is distributed across different wave vectors \mathbf{q} and frequencies ω . The summation over α accounts for the three spatial dimensions (x , y , z), while $\dot{\mathbf{u}}_\alpha(n_{x,y,z}, b; t)$ denotes the time derivative of atomic displacements along the direction α in the unit cell indexed by $n_{x,y,z}$ at time t .

B. First-principles lattice dynamics

In our study, we also utilized a first-principles lattice dynamics (LD) approach for determining the phonon properties of Gd assuming its ferromagnetic ground state and that the fluctuation of the magnetic moments is ignored. This approach does not capture phonon-magnon scattering, in contrast to the SLD approach, and thus overestimates the phononic thermal conductivity. The first-principles calculations were conducted using the Vienna Ab initio Simulation Package (VASP) [43,44], with the projector augmented wave (PAW) potentials [45]. The valence electron configuration for Gd consists of $5s^2 5p^6 4f^7 5d^1 6s^2$ orbitals. We employed a plane-wave basis set at a kinetic energy cutoff of 400 eV, and applied Gaussian smearing with a width of 0.02 eV for

the electronic states. For the Brillouin zone integration of the unit cell, a dense Monkhorst-Pack [46] \mathbf{k} -point mesh of $18 \times 18 \times 9$ was used to ensure convergence. The convergence thresholds were stringently set to 1×10^{-8} eV for the total energy and 0.01 eV/Å for the Hellmann-Feynman forces on each atom. The calculations incorporated the Perdew-Burke-Ernzerhof (PBE) exchange-correlation functional [47]. Furthermore, the on-site Coulomb interaction U for the Gd $4f$ orbitals was treated using the spherically averaged density functional theory (DFT)+ U approach [48], where the Hamiltonian is solely dependent on the effective Coulomb repulsion U , which was set to 6 eV. With this setup, Gd exhibits a ferromagnetic ground state, and its spin moment is $7.4 \mu_B$ per Gd atom, reflecting a high spin state with a half-filled $4f$ shell.

The calculations of Gd phonon properties were carried out using PHONOPY [49], based on the Hellmann-Feynman forces [50]. The interatomic force constants (IFCs) for these calculations were obtained from VASP. We utilized 64-atom supercells with dimensions of $4 \times 4 \times 2$ from the primitive cell and a Γ -centered $3 \times 3 \times 3$ \mathbf{k} -mesh grid for finite-displacement calculations, applying the atomic displacement amplitude of 0.01 Å. For the calculation of the phononic thermal conductivity κ_{ph} , we solved the phonon Boltzmann transport equation iteratively using SHENGBTE, which included the isotopic effect [51]. The thermal conductivity calculation needs the third-order IFCs, and the details were kept consistent with the second-order calculations. In addition, the generation of third-order IFCs involves four neighboring atoms and 84 finite-displacement jobs, equivalent to a 5.8403 Å radius cutoff. A $20 \times 20 \times 20$ mesh is employed for the phonon \mathbf{q} -grid sampling. The convergence test for a denser \mathbf{q} -mesh grid shows less than $0.05 \text{ W m}^{-1} \text{ K}^{-1}$ variation in thermal conductivity.

For the calculation of the Lorenz number, we utilized the linearized Boltzmann transport equation with BOLTZTRAP [52,53]. This method invokes the constant relaxation time approximation (CRTA) in the collision term of the equation. The calculation began with the PBE + U electronic band structure obtained from a Γ -centered $50 \times 50 \times 25$ \mathbf{k} grid. Further refinement was achieved by Fourier interpolating the Fermi surface on a denser Γ -centered $97 \times 97 \times 53$ \mathbf{k} grid.

IV. RESULTS AND DISCUSSIONS

The thermal conductivity of single-crystalline Gd was measured using a customized steady-state method setup, as shown in Fig. 1(a), with further details provided in Sec. II. The magnetic field is applied along the hexagonal c axis. The thermal conductivity and the electrical resistivity are also measured along the c axis. As shown in Fig. 1(b), the temperature-dependent thermal conductivity in the absence of an applied magnetic field exhibits a trend that is consistent with previously reported data [25]. Specifically, the thermal conductivity decreases from 15.8 W/mK at 100 K to approximately 10.8 W/mK around its Curie temperature T_c of 293 K, a reduction attributable to increased phonon-phonon scattering. Notably, the observed increase in thermal conductivity above T_c deviates from the typical behavior expected in crystalline solids, suggesting unusual behaviors of the microscopic heat carriers.

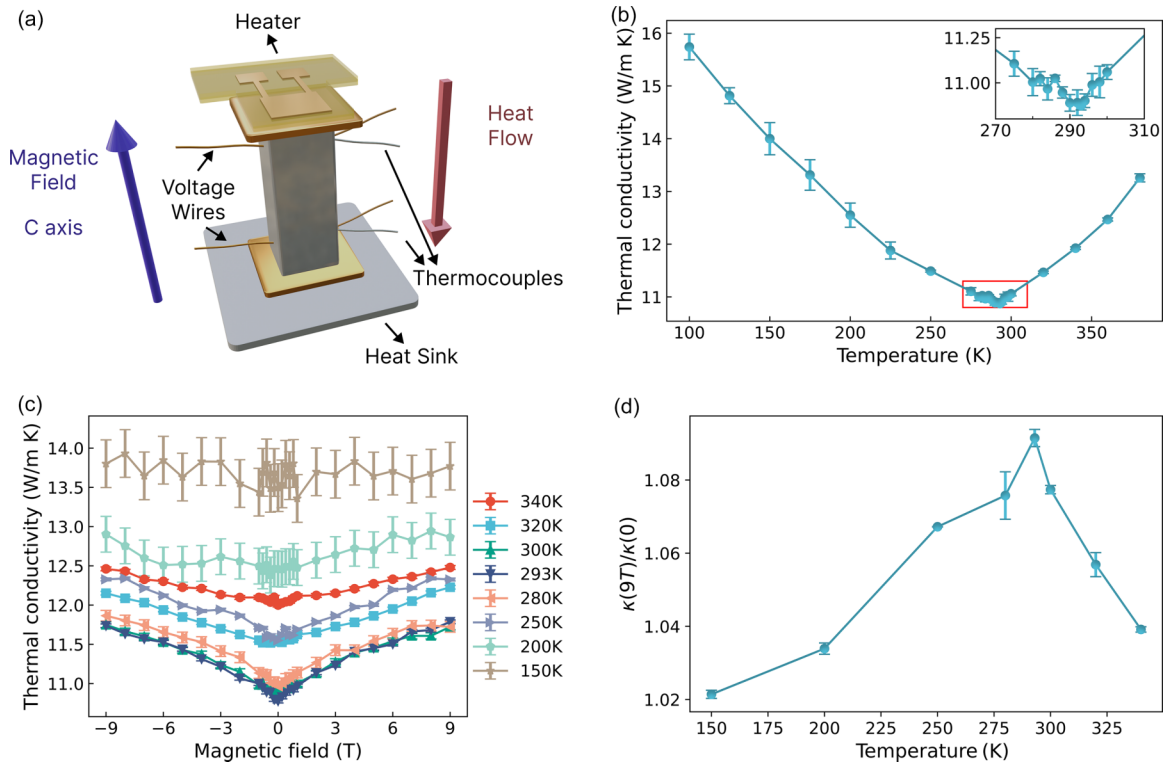


FIG. 1. (a) The schematic of the experimental setup. (b) Measured thermal conductivity of single-crystalline Gd as a function of temperature without an external field. The inset shows the data near the Curie temperature. The thermal conductivity shows a minima around its Curie temperature (293 K). (c) Measured thermal conductivity of single-crystalline Gd as a function of the external magnetic field at different temperatures. The external magnetic field increases the thermal conductivity near the Curie temperature. (d) The switching ratio of the thermal conductivity of Gd under a 9 T magnetic field. Error bars represent random uncertainties from three repeated measurements. More discussion of the random and systematic errors in our measurements is provided in Appendix A.

Magnetic-field-dependent thermal conductivity measurements were conducted at various temperatures, both near (280, 293, and 300 K) and significantly distant from (150, 200, 250, 320, and 340 K) the Curie temperature, with magnetic field strengths of up to 9 T, as illustrated in Fig. 1(c). Near T_c , the thermal conductivity increases with the strength of the external magnetic field, rising from 10.75 W/m K with zero field to 11.6 W/m K under a 9 T magnetic field. This field dependence decreases at temperatures away from T_c and diminishes at 150 K. Consequently, as illustrated in Fig. 1(d), the thermal conductivity switching ratio attains a maximum of 1.09 at the Curie temperature.

Thermal transport in metallic Gd can be mediated by electrons, phonons, and magnons. Since the population of magnons is suppressed by the magnetic field [54], the magnonic thermal conductivity is expected to decrease with the field, contrary to our observation. Furthermore, previous studies have suggested that the contribution of magnons in Gd at room temperature is negligible [25]. Therefore, we focus on analyzing the field dependence of electronic and phononic thermal conductivity.

To estimate the electronic contribution to the thermal conductivity, the magnetoresistance of the same Gd sample was measured. The electrical resistance of the sample as a function of temperature without an external field is provided in Fig. 2(a), showing a typical metallic behavior and good agree-

ment with the literature [55]. As depicted in Fig. 2(b), the sample exhibits a linear negative magnetoresistance, a result of suppressed spin-electron scattering as the local magnetic moments are aligned by the applied external magnetic field, in agreement with previous reports [56,57]. In particular, we found that the magnetoresistance is higher at lower temperature compared to that near the Curie temperature, a similar trend reported previously along the c axis [56]. This behavior is in contrast to the observed magnetic field dependence of the thermal conductivity, which is maximized near the Curie temperature. Based on the Wiedemann-Franz law, which remains applicable in a magnetic field [58], the electronic thermal conductivity can be calculated from the magnetoresistance results. Using the electronic band structure of Gd calculated from first-principles with the density functional theory (DFT), the Lorenz number in Gd is calculated to be very close to the classical value of $2.44 \times 10^{-8} \text{ V}^2 \text{ K}^{-2}$ in the temperature range of our experiment (see Fig. 4 in the Appendix). Although our DFT calculation assumes a ferromagnetic ground state and does not capture the effect of spin fluctuations at finite temperatures on the Lorenz number, we do not expect the Lorenz number in Gd to significantly deviate from the classical value, a scenario that typically occurs in low-dimensional conductors [59] and strongly correlated electronic systems [60,61]. The calculated electronic thermal conductivity based on this Lorenz number is shown in Fig. 2(c). The phononic

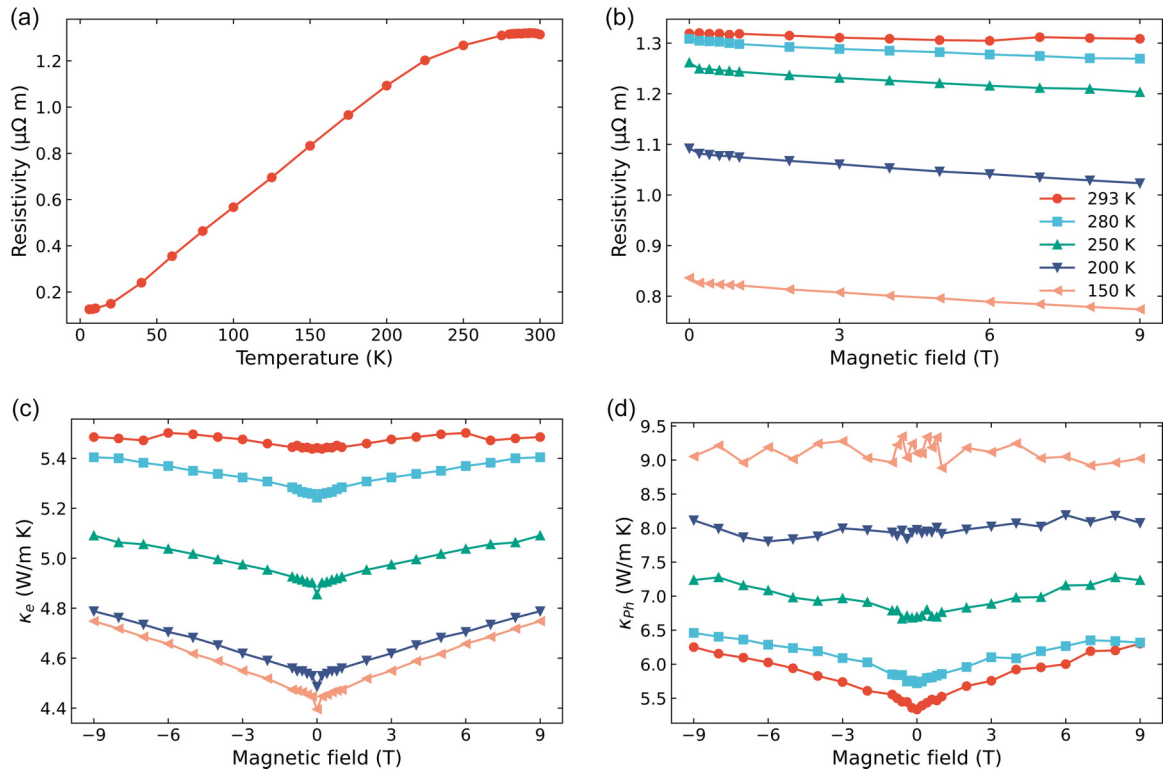


FIG. 2. (a) Measured electrical resistivity of the single-crystal Gd as a function of temperature without a magnetic field. The resistivity shows a general metal trend consistent with previously reported data. (b) The measured electrical resistance of single-crystalline Gd as a function of an external magnetic field at different temperatures. A negative magnetoresistance is measured at all temperatures. A small up-turn of the resistance at 293 K and 7 T is within the uncertainty of the measurement. (c) The electronic thermal conductivity of Gd as a function of an external magnetic field at different temperatures. The electronic thermal conductivity is calculated by applying the Wiedemann-Franz law to the electrical resistivity data. (d) The phononic contribution to the thermal conductivity of single-crystalline Gd as a function of an external magnetic field at different temperatures. The phononic contribution is estimated by subtracting the electronic contribution from the total thermal conductivity using the Wiedemann-Franz law.

thermal conductivity can then be isolated by subtracting the electronic contribution from the total thermal conductivity. The result is depicted in Fig. 2(d). Similar to the total thermal conductivity, the magnetic-field-induced change in the phononic thermal conductivity peaks near the Curie temperature T_c . This result is in sharp contrast to the work by Glorieux *et al.* [36], where the field dependence was fully attributed to the electronic contribution.

Typically, phonons are not expected to directly interact with external magnetic fields due to their nonmagnetic nature. However, it has been proposed that phonons can indirectly respond to such fields through spin-lattice coupling, affecting either phonon-phonon [20] or phonon-magnon scatterings [62,63]. Given prior simulations that show only slight variations in the phonon-dispersion relation in Gd under magnetic fields [34], we hypothesize that the marked field dependence of the phononic thermal conductivity is mainly attributable to the reduction in phonon-magnon scattering instead of changes in the phonon group velocity, phononic heat capacity, or phonon-phonon scattering. Below the Curie temperature T_c , the thermal fluctuations of the local magnetic moments are suppressed by the external magnetic field because the moments tend to align with the field. Equivalently, the magnon population is reduced by the external magnetic field. This can be seen from the equilibrium Bose-Einstein distribution that

the magnons obey [54]:

$$f_0(\omega) = \frac{1}{\exp\left(\frac{\hbar\omega + g\mu_B B}{k_B T}\right) - 1}, \quad (4)$$

where ω is the magnon frequency, g is the Landé g factor, μ_B is the Bohr magneton, B is the external magnetic field, k_B is the Boltzmann constant, and T is the temperature. This effect is also reflected in the quenching of the heat capacity by the applied magnetic field, i.e., the magnetocaloric effect [64]. Thus, the reduction of the magnon population due to an external magnetic field leads to reduced scattering of heat-carrying phonons by magnons, giving rise to an increased phononic thermal conductivity with an applied field. In particular, this effect is maximized near the Curie temperature T_c , where the thermal fluctuations and the exchange interactions of the spins approximately balance each other. As a result, the application of a magnetic field near T_c produces the largest change in the magnetization and, thus, the magnon population [65].

To verify our hypothesis and elucidate the mechanisms underlying the modulation of phononic thermal conductivity, we have employed first-principles lattice dynamics (LD) and spin-lattice dynamics (SLD) simulations to quantitatively explain our experimental results. Details of the calculations are summarized in Sec. III. Briefly, in the LD approach [66],

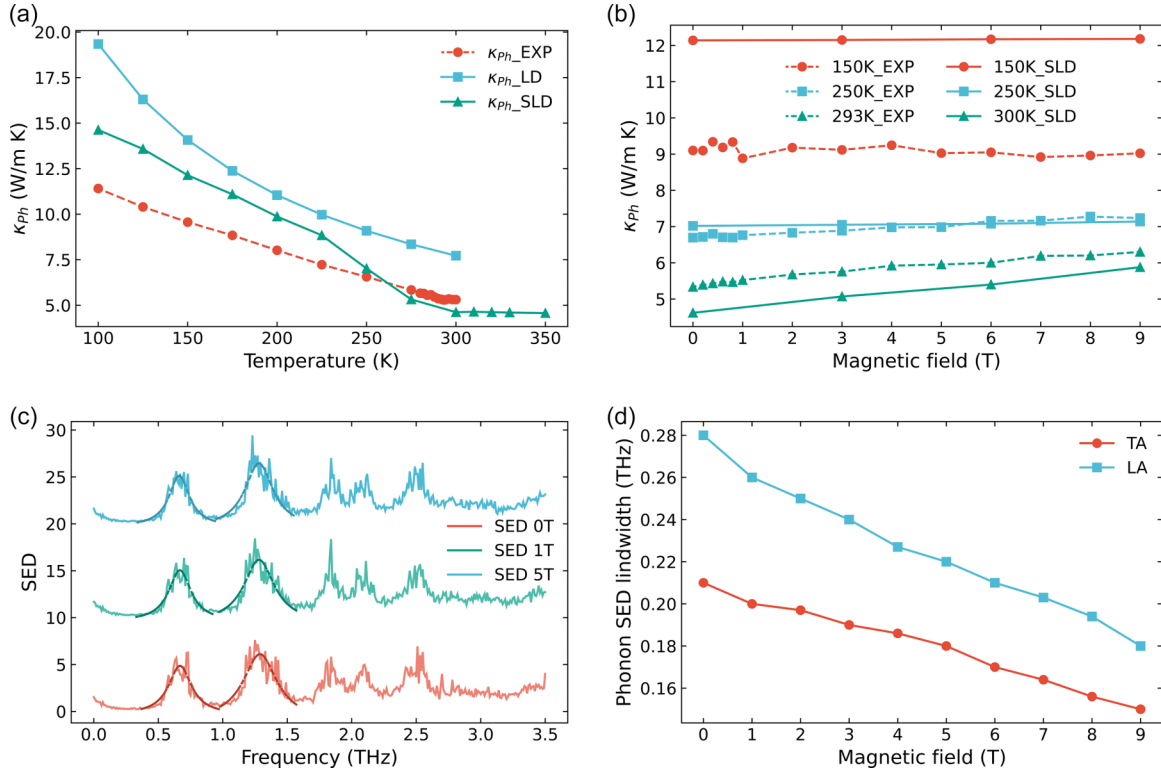


FIG. 3. (a) Comparison of the experimentally measured phononic thermal conductivity of single-crystalline Gd without an external magnetic field (κ_{ph_EXP}) to the results from first-principles lattice dynamics (κ_{ph_LD}) and spin-lattice dynamics (κ_{ph_SLD}) simulations. (b) Comparison of the experimentally measured magnetic field dependence of the phononic thermal conductivity in single-crystalline Gd to the spin-lattice dynamics simulation results at different temperatures. The T_c simulated from SLD is 300 K, while the T_c obtained from experiments is 293 K. (c) The phonon spectral energy density (SED) evaluated at $\mathbf{q} = [0.25, 0, 0]$ from the SLD simulation as a function of an external magnetic field. The two lowest peaks, corresponding to the TA and LA acoustic modes, are fitted to a Lorentzian function to extract their linewidths. (d) The extracted peak linewidth of the TA and LA modes in single-crystalline Gd from the SLD simulation as a function of an external magnetic field up to 9 T. The observed narrowing of the SED peak linewidth in the presence of an external magnetic field suggests suppression of phonon scattering by the field.

the interatomic force constants (IFCs) are calculated at 0 K using DFT for the ferromagnetic ground state of Gd. These IFCs are used to compute the phonon-dispersion relation and phonon-phonon scattering rates at finite temperatures, from which the phononic thermal conductivity can be calculated.

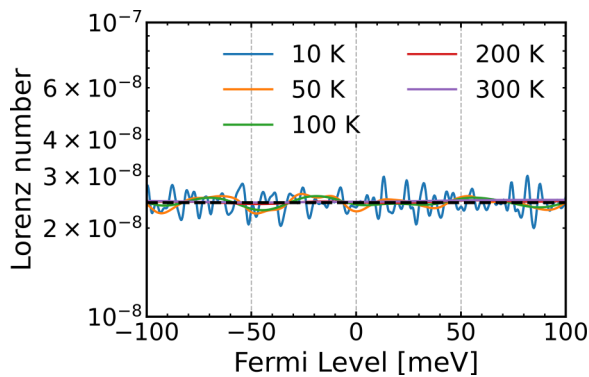


FIG. 4. Calculated Lorenz number in Gd at different temperatures using DFT within the constant relaxation time approximation. The black dashed horizontal line indicates the reference value of the Lorenz number, $2.44 \times 10^{-8} \text{ V}^2 \text{ K}^{-2}$.

Within this approach, the spin degree of freedom is frozen and the phonon-magnon scattering is not captured. The calculated phononic thermal conductivity based on the LD simulation up to the Curie temperature is shown in Fig. 3(a). As expected, the LD simulation provides a theoretical maximum value that is significantly higher than our experimental result, indicating the potentially important role of phonon-magnon scattering. In contrast, in the SLD simulation, both the spin and the lattice degrees of freedom are allowed to fluctuate at a given temperature, with the spin exchange coefficients and interatomic potentials obtained from first-principles using DFT. With the SLD approach, the phonon-magnon scattering is fully captured by taking into account the dependence of the spin exchange interaction on the interatomic distance [34,67]. As shown in Fig. 3(a), when incorporating phonon-magnon interactions through the SLD simulation, the calculated κ_{ph} aligns more closely with the experimental data below the Curie temperature. The small discrepancy between SLD and the experimental results might be due to defect scatterings in the sample. The difference between the LD and SLD results indicates the contribution of phonon-magnon scattering in the determination of the thermal conductivity of Gd. Notably, the SLD simulation predicts an almost temperature-independent phononic thermal conductivity above the Curie

temperature, likely due to the balance between the phonon-phonon and phonon-magnon scatterings. This result suggests that phonon-magnon interaction cannot explain the increase in thermal conductivity with temperature in Gd above T_c shown in Fig. 1(b), which may have an electronic origin [55]. Nevertheless, the SLD simulation successfully and effectively replicates the experimental field dependence observed in the phononic thermal conductivity below T_c , as shown in Fig. 3(b). In particular, the maximum switching effect near T_c is captured in the SLD simulation. To obtain a microscopic understanding of the field-suppressed phonon-magnon scattering, we calculated the peak linewidth of the phonon spectral energy density (SED) at T_c under different external magnetic fields from the trajectories of the ionic motion in the SLD simulation [42]. The peak linewidth is inversely proportional to the lifetime of the corresponding phonon modes, including contributions from both phonon-phonon and phonon-magnon scatterings. As shown in Figs. 3(c) and 3(d), the peak linewidths associated with the transverse acoustic (TA) and the longitudinal acoustic (LA) phonon modes decrease monotonically with the applied external magnetic field. This result provides direct evidence that the total phonon scattering rates are reduced as a result of the applied magnetic field, leading to increased phononic thermal conductivity.

V. CONCLUSION

In summary, we utilized a customized steady-state measurement system to investigate the thermal and electrical magnetoconductivity properties of single-crystalline Gd at various temperatures. Our findings reveal a notable increase in the phononic thermal conductivity with an external magnetic field, a phenomenon particularly pronounced near the Curie temperature. To explore the origin of this field dependence, we implemented first-principles LD and SLD simulations. These simulations pointed to the suppression of phonon-magnon scattering as the primary factor contributing to the observed increase in the phononic thermal conductivity. Our study paves the way for the development of innovative thermal switching materials driven by an external magnetic field, especially those exhibiting strong spin-lattice interactions such as magnetocaloric materials with first-order magnetic phase transitions [68], opening new possibilities in the field of material science and thermal engineering.

ACKNOWLEDGMENTS

The authors acknowledge the help with the SED analysis from X. Wu. This work is based on research supported by the U.S. Office of Naval Research under the Award No. N00014-22-1-2262. Transport measurements were done at UCSB Materials Research Laboratory (MRL) Shared Experimental Facilities, which are supported by the NSF MRSEC Program under Award No. DMR-2308708. The development of the spin-lattice dynamics simulation is supported by the National Aeronautics and Space Administration (NASA) under Award No. 80NSSC21K1812. Y.C. also acknowledges the support from the Graduate Traineeship Program of the NSF Quantum Foundry via the Q-AMASE-i program under Award No. DMR-1906325 at the University of

California, Santa Barbara (UCSB). This work used Stampede2 at Texas Advanced Computing Center (TACC) and Expanse at San Diego Supercomputer Center (SDSC) through allocation MAT200011 from the Advanced Cyberinfrastructure Coordination Ecosystem: Services & Support (ACCESS) program, which is supported by National Science Foundation Grants No. 2138259, No. 2138286, No. 2138307, No. 2137603, and No. 2138296. Use was also made of computational facilities purchased with funds from the National Science Foundation (Grant No. CNS-1725797) and administered by the Center for Scientific Computing (CSC). The CSC is supported by the California NanoSystems Institute and the Materials Research Science and Engineering Center (MRSEC; NSF DMR Grant No. 2308708) at UCSB.

APPENDIX A: ESTIMATING ERRORS IN THERMAL CONDUCTIVITY MEASUREMENT

The measured thermal conductivity was calculated by

$$\kappa = \frac{(IV - Q_{\text{rad}} - Q_{\text{tc}}) \times L}{A \times \Delta T}, \quad (\text{A1})$$

where I is the current supplied to the heater, V is the measured voltage across the heater, and Q_{rad} and Q_{tc} represent the heat loss due to radiation and conduction through the thermocouples, respectively. A represents the cross-section area of the sample. The L and ΔT are the length and temperature difference between the two thermocouples, respectively. Given that direct measurement of the heat flux is unfeasible, we estimate the net heat conducted through the sample by calculating the power (IV) dissipated in the heater resistor and subtracting the losses attributed to radiation and thermal conduction down the thermocouples. The quantities Q_{rad} and Q_{tc} represent the heat loss due to radiation and conduction through the thermocouples, respectively. The radiation heat loss was estimated by

$$Q_{\text{rad}} = \sigma_{\text{T}} \times (S/2) \times \varepsilon \times (T_{\text{hot}}^4 - T_{\text{cold}}^4), \quad (\text{A2})$$

where $\sigma_{\text{T}} = 5.67 \times 10^{-8} \text{ W m}^{-2} \text{ K}^{-4}$ is the Stefan-Boltzmann constant, ε is the infrared emissivity of the radiating surface S is the total sample surface area, and $T_{\text{hot/cold}}$ are the temperature at the hot side and cold side. The total heat losses were calculated to be less than 3%. The primary sources of error in thermal conductivity measurements include sample geometry uncertainty, which is on the order of 10%. It is worth noting that even though the absolute uncertainty is near 10%, the relative error in measuring the change in the thermal conductivity due to magnetic fields is much smaller for the same sample. Additionally, since all data are acquired from the same sample, the systematic error 10% should be considered as an offset rather than the error bar. Thus, we used the standard deviation from three measurements, which represents the random error, as the basis for the error bars in the figures presented in our manuscript.

APPENDIX B: COMPUTATIONAL ESTIMATION OF THE LORENZ NUMBER IN Gd

The Lorenz number in Gd in its ferromagnetic state is estimated using the exact electronic structure of Gd calculated

by DFT (as detailed in the main text). The calculated result as a function of temperature and Fermi level position is shown in

Fig. 4 and is very close to the classical value. It is noted that the spin fluctuation effect is not captured in this calculation.

- [1] G. Wehmeyer, T. Yabuki, C. Monachon, J. Wu, and C. Dames, Thermal diodes, regulators, and switches: Physical mechanisms and potential applications, *Appl. Phys. Rev.* **4**, 041304 (2017).
- [2] P. J. Shirron, M. J. DiPirro, M. Jirmanus, Z. Zhao, and B. Shields, A portable, cryogen-free ultra-low temperature cooling system using a continuous ADR, in *AIP Conference Proceedings*, Vol. 710 (American Institute of Physics, 2004), pp. 1746–1753.
- [3] A. E. Jahromi and D. F. Sullivan, A piezoelectric cryogenic heat switch, *Rev. Sci. Instrum.* **85**, 065118 (2014).
- [4] M. Hao, J. Li, S. Park, S. Moura, and C. Dames, Efficient thermal management of Li-ion batteries with a passive interfacial thermal regulator based on a shape memory alloy, *Nat. Energy* **3**, 899 (2018).
- [5] S. A. Atouei, A. Rezanian, A. Ranjbar, and L. A. Rosendahl, Protection and thermal management of thermoelectric generator system using phase change materials: An experimental investigation, *Energy* **156**, 311 (2018).
- [6] K. Aryana, J. A. Tomko, R. Gao, E. R. Hoglund, T. Mimura, S. Makarem, A. Salanova, M. S. B. Hoque, T. W. Pfeifer, D. H. Olson *et al.*, Observation of solid-state bidirectional thermal conductivity switching in antiferroelectric lead zirconate PbZrO_3 , *Nat. Commun.* **13**, 1573 (2022).
- [7] J. F. Ihlefeld, B. M. Foley, D. A. Scrymgeour, J. R. Michael, B. B. McKenzie, D. L. Medlin, M. Wallace, S. Trolier-McKinstry, and P. E. Hopkins, Room-temperature voltage tunable phonon thermal conductivity via reconfigurable interfaces in ferroelectric thin films, *Nano Lett.* **15**, 1791 (2015).
- [8] C. Liu, Y. Si, H. Zhang, C. Wu, S. Deng, Y. Dong, Y. Li, M. Zhuo, N. Fan, B. Xu *et al.*, Low voltage-driven high-performance thermal switching in antiferroelectric PbZrO_3 thin films, *Science* **382**, 1265 (2023).
- [9] B. L. Wooten, R. Iguchi, P. Tang, J. S. Kang, K.-i. Uchida, G. E. Bauer, and J. P. Heremans, Electric field-dependent phonon spectrum and heat conduction in ferroelectrics, *Sci. Adv.* **9**, eadd7194 (2023).
- [10] M. Li, H. Wu, E. M. Avery, Z. Qin, D. P. Goronzy, H. D. Nguyen, T. Liu, P. S. Weiss, and Y. Hu, Electrically gated molecular thermal switch, *Science* **382**, 585 (2023).
- [11] J. Kimling, R. B. Wilson, K. Rott, J. Kimling, G. Reiss, and D. G. Cahill, Spin-dependent thermal transport perpendicular to the planes of Co/Cu multilayers, *Phys. Rev. B* **91**, 144405 (2015).
- [12] Q. Lu, S. Huberman, H. Zhang, Q. Song, J. Wang, G. Vardar, A. Hunt, I. Waluyo, G. Chen, and B. Yildiz, Bi-directional tuning of thermal transport in SrCoO_x with electrochemically induced phase transitions, *Nat. Mater.* **19**, 655 (2020).
- [13] T. Zhang and T. Luo, High-contrast, reversible thermal conductivity regulation utilizing the phase transition of polyethylene nanofibers, *ACS Nano* **7**, 7592 (2013).
- [14] R. Shrestha, Y. Luan, S. Shin, T. Zhang, X. Luo, J. S. Lundh, W. Gong, M. R. Bockstaller, S. Choi, T. Luo *et al.*, High-contrast and reversible polymer thermal regulator by structural phase transition, *Sci. Adv.* **5**, eaax3777 (2019).
- [15] J. Shin, J. Sung, M. Kang, X. Xie, B. Lee, K. M. Lee, T. J. White, C. Leal, N. R. Sottos, P. V. Braun *et al.*, Light-triggered thermal conductivity switching in azobenzene polymers, *Proc. Natl. Acad. Sci. USA* **116**, 5973 (2019).
- [16] A. Sood, F. Xiong, S. Chen, H. Wang, D. Selli, J. Zhang, C. J. McClellan, J. Sun, D. Donadio, Y. Cui *et al.*, An electrochemical thermal transistor, *Nat. Commun.* **9**, 4510 (2018).
- [17] G. Zhu, J. Liu, Q. Zheng, R. Zhang, D. Li, D. Banerjee, and D. G. Cahill, Tuning thermal conductivity in molybdenum disulfide by electrochemical intercalation, *Nat. Commun.* **7**, 13211 (2016).
- [18] J. A. Tomko, A. Pena-Francesch, H. Jung, M. Tyagi, B. D. Allen, M. C. Demirel, and P. E. Hopkins, Tunable thermal transport and reversible thermal conductivity switching in topologically networked bio-inspired materials, *Nat. Nanotechnol.* **13**, 959 (2018).
- [19] K. Hirata, K. Kuga, M. Matsunami, M. Zhu, J. P. Heremans, and T. Takeuchi, Magneto-thermal conductivity effect and enhanced thermoelectric figure of merit in Ag_2Te , *AIP Adv.* **13**, 015016 (2023).
- [20] H. Jin, O. D. Restrepo, N. Antolin, S. R. Boona, W. Windl, R. C. Myers, and J. P. Heremans, Phonon-induced diamagnetic force and its effect on the lattice thermal conductivity, *Nat. Mater.* **14**, 601 (2015).
- [21] I. Stockem, A. Bergman, A. Glensk, T. Hickel, F. Körmann, B. Grabowski, J. Neugebauer, and B. Alling, Anomalous phonon lifetime shortening in paramagnetic CrN caused by spin-lattice coupling: A combined spin and *ab initio* molecular dynamics study, *Phys. Rev. Lett.* **121**, 125902 (2018).
- [22] C. Kittel and P. McEuen, *Introduction to Solid State Physics* (Wiley, New York, 2018).
- [23] R. Douglass, Heat transport by spin waves in yttrium iron garnet, *Phys. Rev.* **129**, 1132 (1963).
- [24] S. R. Boona and J. P. Heremans, Magnon thermal mean free path in yttrium iron garnet, *Phys. Rev. B* **90**, 064421 (2014).
- [25] P. Jacobsson and B. Sundqvist, Thermal conductivity and electrical resistivity of gadolinium as functions of pressure and temperature, *Phys. Rev. B* **40**, 9541 (1989).
- [26] C. Bhandari and G. Verma, Scattering of magnons and phonons in the thermal conductivity of yttrium iron garnet, *Phys. Rev.* **152**, 731 (1966).
- [27] D. Sanders and D. Walton, Effect of magnon-phonon thermal relaxation on heat transport by magnons, *Phys. Rev. B* **15**, 1489 (1977).
- [28] X. Zhao, J. Wu, Z. Zhao, Z. He, J. Song, J. Zhao, X. Liu, X. Sun, and X. Li, Heat switch effect in an antiferromagnetic insulator $\text{Co}_3\text{V}_2\text{O}_8$, *Appl. Phys. Lett.* **108**, 242405 (2016).
- [29] X. M. Wang, C. Fan, Z. Y. Zhao, W. Tao, X. G. Liu, W. P. Ke, X. Zhao, and X. F. Sun, Large magnetothermal conductivity of HoMnO_3 single crystals and its relation to the magnetic-field-induced transitions of magnetic structure, *Phys. Rev. B* **82**, 094405 (2010).
- [30] Q. J. Li, Z. Y. Zhao, C. Fan, F. B. Zhang, H. D. Zhou, X. Zhao, and X. F. Sun, Phonon-glass-like behavior of magnetic origin in single-crystal $\text{Tb}_2\text{Ti}_2\text{O}_7$, *Phys. Rev. B* **87**, 214408 (2013).

- [31] K. Berggold, J. Baier, D. Meier, J. A. Mydosh, T. Lorenz, J. Hemberger, A. Balbashov, N. Aliouane, and D. N. Argyriou, Anomalous thermal expansion and strong damping of the thermal conductivity of NdMnO₃ and TbMnO₃ due to 4f crystal-field excitations, *Phys. Rev. B* **76**, 094418 (2007).
- [32] Y. Ando, J. Takeya, D. L. Sisson, S. G. Doettinger, I. Tanaka, R. S. Feigelson, and A. Kapitulnik, Thermal conductivity of the spin-Peierls compound CuGeO₃, *Phys. Rev. B* **58**, R2913 (1998).
- [33] K. Kawasaki, On the behavior of thermal conductivity near the magnetic transition point, *Prog. Theor. Phys.* **29**, 801 (1963).
- [34] L. Patra and B. Liao, Indirect exchange interaction leads to large lattice contribution to magnetocaloric entropy change, *Phys. Rev. Lett.* **131**, 066703 (2023).
- [35] S. Aarjts and R. Colvin, Thermal conductivity and Lorenz function of gadolinium between 5 and 310 K, *J. Appl. Phys.* **35**, 1043 (1964).
- [36] C. Glorieux, J. Thoen, G. Bednarz, M. A. White, and D. J. W. Geldart, Photoacoustic investigation of the temperature and magnetic-field dependence of the specific-heat capacity and thermal conductivity near the Curie point of gadolinium, *Phys. Rev. B* **52**, 12770 (1995).
- [37] J. Jensen and A. R. Mackintosh, *Rare Earth Magnetism* (Clarendon Press, Oxford, 1991).
- [38] J. Tranchida, S. J. Plimpton, P. Thibaudeau, and A. P. Thompson, Massively parallel symplectic algorithm for coupled magnetic spin dynamics and molecular dynamics, *J. Comput. Phys.* **372**, 406 (2018).
- [39] H. Ebert, D. Koedderitzsch, and J. Minar, Calculating condensed matter properties using the KKR-Green's function method—Recent developments and applications, *Rep. Prog. Phys.* **74**, 096501 (2011).
- [40] H. Ebert, J. Minar, and V. Popescu, The Munich SPR-KKR Package (2012), https://www.ebert.cup.uni-muenchen.de/old/index.php?option=com_content&view=article&id=8&catid=4&Itemid=7&lang=en.
- [41] J. A. Thomas, J. E. Turney, R. M. Iutzi, C. H. Amon, and A. J. H. McGaughey, Predicting phonon dispersion relations and lifetimes from the spectral energy density, *Phys. Rev. B* **81**, 081411(R) (2010).
- [42] X. Wu, Z. Liu, and T. Luo, Magnon and phonon dispersion, lifetime, and thermal conductivity of iron from spin-lattice dynamics simulations, *J. Appl. Phys.* **123**, 085109 (2018).
- [43] G. Kresse and J. Furthmüller, Efficient iterative schemes for *ab initio* total-energy calculations using a plane-wave basis set, *Phys. Rev. B* **54**, 11169 (1996).
- [44] G. Kresse and J. Furthmüller, Efficiency of *ab initio* total energy calculations for metals and semiconductors using a plane-wave basis set, *Comput. Mater. Sci.* **6**, 15 (1996).
- [45] P. E. Blöchl, Projector augmented-wave method, *Phys. Rev. B* **50**, 17953 (1994).
- [46] H. J. Monkhorst and J. D. Pack, Special points for Brillouin-zone integrations, *Phys. Rev. B* **13**, 5188 (1976).
- [47] J. P. Perdew, K. Burke, and M. Ernzerhof, Generalized gradient approximation made simple, *Phys. Rev. Lett.* **77**, 3865 (1996).
- [48] S. L. Dudarev, G. A. Botton, S. Y. Savrasov, C. J. Humphreys, and A. P. Sutton, Electron-energy-loss spectra and the structural stability of nickel oxide: An LSDA+*U* study, *Phys. Rev. B* **57**, 1505 (1998).
- [49] A. Togo and I. Tanaka, First principles phonon calculations in materials science, *Scr. Mater.* **108**, 1 (2015).
- [50] R. P. Feynman, Forces in molecules, *Phys. Rev.* **56**, 340 (1939).
- [51] W. Li, J. Carrete, N. A. Katcho, and N. Mingo, ShengBTE: A solver of the Boltzmann transport equation for phonons, *Comput. Phys. Commun.* **185**, 1747 (2014).
- [52] G. K. Madsen and D. J. Singh, BoltzTraP. A code for calculating band-structure dependent quantities, *Comput. Phys. Commun.* **175**, 67 (2006).
- [53] G. K. Madsen, J. Carrete, and M. J. Verstraete, BoltzTraP2, A program for interpolating band structures and calculating semiclassical transport coefficients, *Comput. Phys. Commun.* **231**, 140 (2018).
- [54] B. Liao, J. Zhou, and G. Chen, Generalized two-temperature model for coupled phonon-magnon diffusion, *Phys. Rev. Lett.* **113**, 025902 (2014).
- [55] H. E. Nigh, S. Legvold, and F. Spedding, Magnetization and electrical resistivity of gadolinium single crystals, *Phys. Rev.* **132**, 1092 (1963).
- [56] T. Hiraoka and M. Suzuki, Magnetoresistance effect in single crystals of Gd, *J. Phys. Soc. Jpn.* **31**, 1361 (1971).
- [57] K. McEwen, G. Webber, and L. Roeland, Magnetoresistance of gadolinium, *Physica B+C* **86-88**, 533 (1977).
- [58] J. Ziman, *Electrons and Phonons* (Oxford University Press, UK, 1960).
- [59] N. Wakeham, A. F. Bangura, X. Xu, J.-F. Mercure, M. Greenblatt, and N. E. Hussey, Gross violation of the Wiedemann-Franz law in a quasi-one-dimensional conductor, *Nat. Commun.* **2**, 396 (2011).
- [60] K. Behnia, R. Bel, Y. Kasahara, Y. Nakajima, H. Jin, H. Aubin, K. Izawa, Y. Matsuda, J. Flouquet, Y. Haga *et al.*, Thermal transport in the hidden-order state of URu₂Si₂, *Phys. Rev. Lett.* **94**, 156405 (2005).
- [61] S. Lee, K. Hippalgaonkar, F. Yang, J. Hong, C. Ko, J. Suh, K. Liu, K. Wang, J. J. Urban, X. Zhang *et al.*, Anomalous low electronic thermal conductivity in metallic vanadium dioxide, *Science* **355**, 371 (2017).
- [62] D. D. Vu, R. A. Nelson, B. L. Wooten, J. Barker, J. E. Goldberger, and J. P. Heremans, Magnon gap mediated lattice thermal conductivity in MnBi₂Te₄, *Phys. Rev. B* **108**, 144402 (2023).
- [63] K. Gofryk, S. Du, C. Stanek, J. Lashley, X.-Y. Liu, R. Schulze, J. Smith, D. Safarik, D. Byler, K. McClellan *et al.*, Anisotropic thermal conductivity in uranium dioxide, *Nat. Commun.* **5**, 4551 (2014).
- [64] A. M. Tishin, K. A. Gschneidner, Jr., and V. K. Pecharsky, Magnetocaloric effect and heat capacity in the phase-transition region, *Phys. Rev. B* **59**, 503 (1999).
- [65] S. Y. Dan'Kov, A. M. Tishin, V. K. Pecharsky, and K. A. Gschneidner, Magnetic phase transitions and the magnetothermal properties of gadolinium, *Phys. Rev. B* **57**, 3478 (1998).
- [66] D. A. Broido, M. Malorny, G. Birner, N. Mingo, and D. Stewart, Intrinsic lattice thermal conductivity of semiconductors from first principles, *Appl. Phys. Lett.* **91**, 231922 (2007).
- [67] P.-W. Ma, C. H. Woo, and S. L. Dudarev, Large-scale simulation of the spin-lattice dynamics in ferromagnetic iron, *Phys. Rev. B* **78**, 024434 (2008).
- [68] F. Guillou, G. Porcari, H. Yibole, N. van Dijk, and E. Brück, Taming the first-order transition in giant magnetocaloric materials, *Adv. Mater.* **26**, 2671 (2014).